Nozzle-Free Liquid Microjetting via Homogeneous Bubble Nucleation

Taehwa Lee, Hyoung Won Baac, Jong G. Ok, Hong Seok Youn, and L. Jay Guo

Phys. Rev. Applied **3**, 044007 — Published 16 April 2015

DOI: 10.1103/PhysRevApplied.3.044007

Nozzle-free Liquid Micro-jetting via Homogeneous Bubble Nucleation

Taehwa Lee[1], Hyoung Won Baac[2], Jong G. Ok[3], Hong Seok Youn[4,5,*], L. Jay Guo[1,4,†]

[1]*Department of Mechanical Engineering, University of Michigan, Ann Arbor, MI 48109, USA*

[2]*School of Electronic and Electrical Engineering, Sungkyunkwan University, Suwon 440-746, Korea*

[3]*Department of Mechanical and Automotive Engineering, Seoul National University of Science and Technology, Seoul 139-743, Korea*

[4]*Department of Electrical Engineering and Computer Science, University of Michigan, Ann Arbor, MI 48109, USA*

[5]*National Center for Nanoprocess and Equipment, Korea Institute of Industrial Technology (KITECH), Gwangju, 500-480, Korea*

Abstract

We propose and demonstrate a new physical mechanism for producing liquid micro-jets by taking an optoacoustic approach that can convert light to sound through a carbon nanotube (CNT)-coated lens, where light from a pulsed laser is converted to high momentum carried by the sound wave. The CNT lens can focus high-amplitude sound waves to a micro-spot of < 100 μm near the air-water interface from the water side, leading to micro-bubbles in water and subsequent micro-jets into the air. Laser-flash shadowgraphy visualizes two consecutive jets closely correlated with bubble dynamics. Due to the acoustic scattering from the interface, negative pressure amplitudes are significantly increased up to 80 MPa, even allowing homogeneous bubble nucleation. As a demonstration, this nozzle-free approach is applied to inject colored liquid into a tissue-mimicking gel as well as print a material on a glass substrate.

PACS numbers: *43.25.Yw,*43.35.Ei / 61.48.De / *43.35.Ud, 78.20.Pa

*Present Address: Department of Mechanical Engineering, Hanbat National University, Daejeon, 305-719, Korea

†Correspondence: guo@umich.edu

I. INTRODUCTION

Liquid jetting accompanied by droplet formation is widely observed in nature. The underlying mechanisms of liquid jetting vary with different driving forces, leading to different characteristics of jets (e.g., jet column width and jet speed). Particular interest has been given to micro-sized liquid jets for applications ranging from needle-free drug injection [1,2] to high-resolution inkjet printing [3]. Among various jetting methods, the simplest one is based on the incompressibility of liquid; a small amount of liquid is pushed out of a nozzle due to the volume change induced by the deformation of a piezoelectric-driven membrane [4] or by the expanding bubble within a liquid container that is thermally generated by a pulsed laser [5], an electric discharger [6], or an electric heater [7]. Alternatively, high-speed jets are produced by an impulsive acceleration that occurs when a tube filled with a liquid falls under its own weight onto a solid surface [8,9]. More recently, Tagawa *et al*. reported supersonic micro-jets (jet speed up to 850 m/s) produced by laser-induced bubbles and consequent shock waves in an open liquid-filled capillary when the liquid surface inside the tube forms a concave meniscus [10].

The aforementioned approaches either require nozzles (or equivalent) to eject liquids from containers or to form a concave liquid meniscus, which makes it vulnerable to nozzle clogging, especially when jetting liquids contain flakes, particles, or surface-adhesive biological molecules (e.g., proteins). Some applications such as drug injection require high-speed jets to penetrate resistive and lipid-rich skins [1]. These call for a nozzle-free high-speed jetting. The existing nozzle-free jetting schemes have shown promise, but they have limitations [1,11-14]. For example, a high intensity acoustic beam can lead to liquid ejection when it is focused to the air-liquid interface, but the jets have relatively slow speed [11]. Earlier work showed that high-speed jets (up to 250 m/s) could be produced by bubble collapse near the air-liquid interface, but in an uncontrolled manner [12]. Recently, jetting of a highly viscous liquid was demonstrated through the interaction between a laser-induced spherical bubble and the air-liquid interface [13,14]. In this process, the bulk liquid needs to be optically transparent to laser light. Moreover, the laser-based method may not be suitable for thermally unstable materials since high temperature can change the material properties (e.g., the efficacy of drugs, especially protein-based materials), limiting its use in some practical applications.

In this work, we demonstrate nozzle-free, high-speed liquid micro-jetting through a non-thermal process by using a short focused acoustic pulse (<100 ns), which is generated by a recently developed carbon-nanotube (CNT) optoacoustic transmitter capable of focusing to a spot the size of approximately 100 μm [15]. High-speed jets (up to 200 m/s) are induced by the impingement of the short acoustic pulse on the air-water interface and subsequent cavitation. Due to the acoustic scattering from the pressure-release boundary, the negative amplitude of the optoacoustic pulse is significantly increased up to 80 MPa, even exceeding the homogeneous nucleation threshold of water. Two types of jets during the process are observed: primary slow jets caused by initial bubble growth and secondary fast jets produced

by bubble collapse. We show two possible applications: liquid printing on a substrate and liquid injection into a tissue-mimicking material.

II. EXPERIMENTAL SETUP

A. Optoacoustic wave generation and jet formation

An experimental setup for liquid jetting and optoacoustic generation is illustrated in Fig. 1(a). Liquid jets into the air are generated by focusing acoustic waves on the air-water interface from the water side. The acoustic waves are produced by means of the optoacoustic effect using an optoacoustic transmitter that consists of a transparent concave lens coated with a carbon nanotube (CNT)-polymer composite (referred to as CNT lens thereafter) [15,16]. The CNT composite, where CNTs are embedded in polydimethylsiloxane (PDMS) elastomer, serves as an excellent light-to-sound converter because the CNTs efficiently absorb an incident optical energy and convert it to heat that is rapidly transferred to the surrounding PDMS with a high thermal expansion coefficient. The acoustic waves, excited by a pulsed Nd:YAG laser beam (Continuum, Surelite I-20, $\lambda = 532$ nm, pulse width = 6 ns), are geometrically focused from the CNT lens (focal length ~ 5.5 mm), producing a pressure pulse with a pulse width (< 100 ns) and a negative pressure amplitude (> 20 MPa).

To prevent from potential contamination of the CNT lens and to minimize acoustic propagation loss (if jetting liquid has high viscosity), we first immerse the CNT lens in deionized water which is then separated from jetting liquids by an acoustically transparent film (plastic wrap; polyvinyl chloride (PVC), 12.5 μm thickness). Water and a water-based blue ink (Artist's Loft, watercolor) are used as jetting liquids, which are supplied through a capillary tube (500 μm inner diameter) by a glass syringe (Micro-Mate, capacity 5 mL) actuated by a manual linear translation stage (Newport). In this system, the liquid level is controlled by the amount of a jetting material supplied by the syringe (see Supplemental Material for figure S1 [17]). For jet printing experiment, we use a glass (Fisher, 500 μm) as a target substrate, which is cleaned in an ultrasonic bath using acetone and isopropyl alcohol (IPA), and then dried with nitrogen gas. For liquid injection demonstration, agarose gel, known as a tissue-mimicking material, is used as a target substrate. The target substrates are controlled by a 3-axis motorized stage.

B. Visualization of jet formation

The jetting process is visualized by the laser-flash shadowgraph technique [18-20], a pulsed pump-probe method that allows a probe laser pulse (N_2-pumped dye laser, FWHM = 1 ns) to obtain images at different temporal moments specified by the time delay between the pump (for exciting optoacoustic wave) and the probe pulses through the delay generator (Stanford Research Systems, DG535). Time-resolved images of the acoustic waves, bubbles, and jets can be captured by a CCD camera (Mightex) in the nanosecond resolution, which is determined by the probe beam with a short exposure time of 1 ns.

The visualization experiment is conducted with two different setups: the air-side setup for examining jetting and the water-side setup for bubble dynamics, as illustrated in Fig. 1(b). This is because significant light scattering from a non-flat liquid meniscus induced by surface tension makes it difficult to monitor phenomena that occur in close proximity of the air-water interface. To correlate the results from two different setups, changes are minimized. For the air-side imaging, the chamber is slightly overfilled with the water, forming the free surface with a concave-down meniscus. For the water-side imaging, after adding water into the same chamber, we only introduce a large air pocket (radius of curvature 2 mm) injected by a glass syringe through a capillary tube (inner diameter 500 μm), while the others including the optics alignment keep unchanged. The air pocket (2 mm) forms the air-water interface with a concave shape and is much larger than the bubbles (200 μm) formed by the focused acoustic waves. To keep the same interface position as that for the air side imaging, the field-of-view of the CCD is used as a reference position. The interface relative to the acoustic focus is then placed by a 3-axis motorized stage capable of moving the capillary with 1 μm resolution.

III. RESULTS AND DISCUSSION

A. Visualization of liquid micro-jets and bubbles

The optoacoustic waves generated by the concave CNT lens propagate in the water toward the air-water interface, impinging on the interface and consequently producing water jets in the air. To examine the jetting process, micro-jets in the air are monitored by the back-illuminating shadowgraphy technique, as the time-resolved images are summarized in Fig. 2(a). At the laser energy E=50 mJ/pulse, two consecutive micro-jets are observed for 15 μs after the impingement of the waves: a primary slow jet and a secondary fast jet. First, the primary jet starts to emerge from the air-water interface 1 μs after the focused optoacoustic pulse arrives at the interface (t=0). The water jet continues to grow until it reaches its maximum height and then the height of the jet decreases, which is in turn followed by the secondary fast jet (t=10 μs) that grows more rapidly than the primary jet. The jet height evolution is plotted in Fig. 3(a), exhibiting two different peaks, each corresponding to the primary and secondary jets, respectively. It is observed that the second peak is higher than the first one, as the height of the secondary jet is higher than that of the primary jet. Moreover, the secondary jet is much faster than the initial jet. As shown in Fig. 3(b), the jet speed linearly increases with laser energy. With laser energies E>50 mJ/pulse, the secondary jets can reach up to 200 m/s, while the primary jets up to 50 m/s.

To elucidate the mechanism underlying the consecutive jet formation, we then visualize the water side at the same laser energy as for the jet imaging (Fig. 2b). The densely-packed bubbles nucleate in the immediate subsurface 100 ns after the short focused pressure pulse hits the air-water interface. The explosive bubble formation, accompanied by the shock wave (marked as S1), can contribute to the primary jet production by pushing the surrounding liquid. Note that the shock wave (S1) originated from the bubble zone can be differentiated from the incoming optoacoustic wave with a larger radius of curvature (t=- 300 ns). The bubble cloud coalesces into a single large bubble with a defined bubble edge, but the bubble

zone remains similar in size until t=6 μs because bubbles can leave the bubble nucleation zone before coalescing (see Supplemental Material for figure S2 [17]). Finally, the bubble collapses at t=10.1 μs, generating a secondary shock wave (S2). By correlating the cavitation images with the jetting images, we find that the bubble collapse coincides with the inception of the secondary jet. This indicates that the secondary fast jet is induced by the bubble collapse, while the primary slow jet is related to initial bubble growth and the impingement of the focused optoacoustic wave. Also, the shrinking bubble may cause the first jet to be pulled back before the second jet emerges, as it cannot be only explained by liquid surface tension (see Supplemental Material for a discussion of surface tension effect [17]). As compared with the bubble growth, the bubble collapse can yield more localized pressure, thus producing the secondary jet with higher speed and smaller column width than the primary jet.

The shape of the air-water interface is important for the jet formation and the bubble hydrodynamics. It has been reported that a concave-up interface (toward the air, ∪) with a smaller radius of curvature can promote the kinematic focusing of the liquid, thus producing high-speed jets, whereas the focusing is lost for the interface with a concave-down shape (∩) [10]. In this work, for the air-side imaging, the liquid interface is almost flat, no significant focusing is expected. In contrast, for the water-side imaging, the liquid interface is noticeably curved, forming a concave-up shape (∪) with a radius of curvature 2 mm (much larger than the bubble zone 200 μm in diameter). To compare with the work above where they examined the effect of contact angle (as the concavity of the interface) on liquid focusing, we estimate the contact angle by assuming a capillary of 400 μm in diameter, which is higher than 80°, possibly leading to reduced liquid focusing. However, what is important is whether the curved surface would significantly change the bubble lifetime. As reported in the literature [21], bubble lifetime (first oscillation) decreases with decreasing radius of curvature. With the radius of curvature obtained from the shadowgraph image, a decrease in the lifetime is calculated to be less than 5% compared to that for the flat interface (see Supplemental Material for the detailed calculation [17]).

The two consecutive jets were similarly observed elsewhere [22] by employing a shock-wave lithotripter for acoustic cavitation. Contrast to our nozzle-free jetting, their approach used a micro-hole in a silicon plate, which not only served as an bubble nucleation site but also as a nozzle to eject a water jet. However, possibly, because of the friction between the water and the micro-hole (500 μm in depth), the jet speed was slower than ours, and the primary jet was overlapped with the secondary jet (referred to as the ring jet in their work). Moreover, our jetting is different from what was observed in laser-induced spherical bubbles interacting with the free surface [13,14]. The thermal bubbles did not generate the secondary jets, but primary slow jets toward the air and simultaneously a counter-jet toward the bulk liquid. This difference may arise because the dynamics of the laser-induced single spherical bubbles is substantially different from that of the non-spherical bubble cloud in this work.

B. Acoustic interference effect and Homogeneous bubble nucleation

Since the jetting process is strongly related to the bubble dynamics in the water, we examine the bubble nucleation by simulating the pressure field in the nucleation zone (bubbles nucleate when the applied pressure amplitude is above the threshold pressure). To calculate the pressure field near the air-water interface, the linear wave equation in a lossless medium is solved by using a finite element method (the Courant number CFL < 0.05; COMSOL Multiphysics 4.3b). For simplicity, the nonlinear wave propagation and attenuation are assumed to be negligible because we focus on the acoustic interference in a small region near the interface (z<200 μm, where z is the distance from the interface). Instead, a proper incident pressure on the optoacoustic lens is chosen to match the measured signal at the focus in the boundary-free field (referred to as free field hereafter). Moreover, the air-water interface is simplified as a non-deformable boundary with an acoustic reflectance of $R = -1$. Although the acoustic wave impinging on the fluid interface can lead to the interface deformation, the non-deformable interface in our case is confirmed by the shadowgraph images indicating no measurable deformation of the interface at the initial stage of bubble growth (later, significant interface deformation occurs when jets emerges from the free surface). Comparably, the interface deformation in a similar pressure range was calculated to be less than 10 μm elsewhere where accurate shock and interface capturing were simulated using multicomponent Euler equation [23].

Figure 4(a) shows the calculated peak negative pressure field (surface plot with contour lines) in water near the free surface, normalized to the maximum negative pressure amplitude in the free field. The blue colored region with high negative amplitudes is laterally confined because of tight focusing of the pressure pulse, which is in good agreement with the measured acoustic spot size of approximately 100 μm. This high-amplitude region is also localized near the interface (z<100 μm). This localization is due to the acoustic interference; the short acoustic wave is reflected from the interface and then is interfered with the rest of the incoming wave. Notably, the blue region with a crescent shape is well matched with the shape of the bubble cloud observed in the shadowgraph image (Fig. 4b), indicating that the bubbles favorably nucleate in the high-amplitude zone.

To further examine the interference effect, the simulated pressure transients for different distances (z) along r=0 are plotted in Fig. 4(c). The dashed signal indicates the free-field optoacoustic signal at the focus that has a bipolar waveform with a leading positive amplitude (P_{f+}), a trailing negative amplitude (P_{f-}), and a peak-to-peak time delay ($\tau \sim 45$ ns). The interference signal transients (solid lines) calculated at different locations (z = 3, 6, 10, 15, 20, 30 μm) carry an additional positive phase (i.e., tri-polar waveforms) due to the acoustic reflection. With increasing the distance z, the signal amplitudes gradually increase. At the locations z>10 μm, the negative amplitudes become higher than that of the free-field, reaching to the maximum value at the distance $z_{\max} = 30$ μm, which corresponds to the sum of the free-field negative and positive amplitudes (i.e., $P_{f+} + P_{f-}$). The maximum location $z_{\max}$ can be calculated using the peak-to-peak time delay τ by $z_{\max} = c\tau/2 \cong 30$ μm (c is the speed of sound) because the maximum occurs when the two peaks of the free-field signal are exactly overlapped. This suggests that the location of the bubble cloud from the interface,

which significantly affects the characteristics of the jetting, can be controlled by the acoustic waveform (more precisely, the peak-to-peak time delay τ). The optoacoustic waveform can be tuned by a laser pulse duration and the thickness of the CNT layer. As shown in Fig. 4(d), the positive and negative peak interference pressure (P_i) are plotted as function of z. Beyond $z_{\max}$, the negative interference pressure amplitudes decrease down to the free-field amplitude, while the positive pressure amplitudes remain constant. As indicated in the plot, the bubble nucleation zone is defined as a region where the interference negative pressure amplitudes are higher than the threshold pressure.

Due to the scattering effect, the negative pressure amplitudes can be significantly increased. Figure 5 shows the peak pressure amplitudes as a function of laser energy. The symbols indicate the free-field pressure amplitudes (circle and square) and the interference pressures (triangle). While the free-field amplitudes are measured by a fiber-optic hydrophone, the interference amplitudes are the estimated values because the hydrophone (125 μm in diameter) is too large to measure the signals at the locations close to the interface (<100 μm). The estimation is made with the free-field pressures by the relation $P_{i-}(z_{\max}) = P_{f+} + P_{f-}$. Moreover, for laser energies higher than 15 mJ/pulse, we also need to estimate the free-field negative amplitudes (P_{f-}) because above the laser energy, cavitation occurs at the tip of the hydrophone, distorting the negative signals. We use the relation of $P_{f-} \cong P_{f+}/2,$ as the dashed line ($P_{f+}/2$) fits to the measured negative amplitudes (by inspection of the free-field signal, the positive amplitude is approximately twice higher than the negative one). The interference pressure can reach up to 80 MPa, even exceeding the homogeneous bubble nucleation threshold (60 MPa [23]). This offers an unique advantage because the jetting enabled by the homogeneous bubble nucleation does not require heterogeneous nucleation sites such as particles and gases, allowing our approach to be widely applicable regardless of the condition of water-based jetting liquids.

The homogenous bubble induced by the CNT lens is tolerable to a change in the free surface level with respect to the position of the acoustic focus. As shown in Fig. 6, by moving the air pocket and thus changing the interface positions relative to the acoustic focus (dashed line), the bubble nucleation zones are visualized. All the bubble images taken at the time t = 4 μs look alike both in size and position from the interface; the position from the interface (i.e., stand-off distance) is predetermined by the optoacoustic waveform (i.e., $z_{max} \sim c\tau/2$), which is valid within an acoustic focal depth of approximately 500 μm. As the stand-off distance is important for the bubble dynamics and jetting, our jetting approach with the fixed stand-off distance becomes controllable and reproducible even when the free surface is slightly fluctuated.

C. Potential applications: liquid injection and printing

Finally, we show two potential applications including printing on a substrate and liquid injection into a material. First, we demonstrate liquid printing on a glass substrate. It is confirmed that the jet characteristics depends on the applied laser energy. At the laser energy E = 32 mJ/pulse, the secondary jet produces a single droplet with approximately 20 μm in

diameter, while the primary jet does not (see Supplemental Material for figure S3 [17]). As shown in Fig. 7(a), liquid droplets are deposited on the glass substrate. The deposited droplets spaced 200 μm apart are formed by applying multiple laser pulses to obtain a sizable liquid droplet. With the motorized system, the letter 'M' is printed on the glass substrate, and its microscope image is shown in Fig. 7(b). The line width is approximately 30 μm, slightly larger than the droplet diameter. The left side of the printed letter with slight liquid splashes is lighter in color than its right side, which is possibly because the distance between the liquid interface and the substrate is varied. The printing quality can be further improved by optimizing several parameters, including laser operating conditions (such as laser pulse energy, repetition rate), substrate moving speed, and more importantly a distance between bubbles and the liquid surface.

Second, using the high-speed jets (up to 200 m/s), we demonstrate liquid injection into a tissue-mimicking gel (agarose gel). For visual confirmation, we use a watercolor blue ink as a drug substitute. Figure 8 shows jet-induced injection of the ink into the gel. The gel with 1 mm thickness is placed right above the air-ink interface. The color ink can penetrate into the material by applying several jets, which is clearly shown as the number N of applied jets increase (N = 0, 1, 2, 3, 10, and 20). It should be noted that our jetting method involving two consecutive jets may have some limitations as a result of the combined effect of the two jets with different characteristics. This effect can be mitigated by choosing the proper distance between the air-liquid interface and the target substrate that is larger than the height of the first jet, but lower than the second jet. Although additional optimization may be necessary for actual skins, this preliminary result demonstrates the feasibility of our approach to needle-free drug injection that requires a significant driving force to penetrate resistive, lipid-rich skins.

IV. CONCLUSION

We have demonstrated a nozzle-free, high-speed liquid micro-jet produced by acoustically generated bubbles near the air-water interface. The micro-bubbles were homogeneously nucleated by a focused nanosecond-long pressure pulse generated by the efficient carbon nanotube (CNT)-based light-to-sound converter. The homogeneous bubble nucleation was enabled by the acoustic scattering of a nanosecond-long pressure pulse from the air-water (pressure-release) boundary. Two consecutive micro-jets were influenced by bubble dynamics: primary slow jet by initial bubble growth and primary fast jet by bubble collapse.

Our approach has several practical advantages. First, this approach can broaden choice of jetting materials. With the nozzle-free method, we can even use materials that contain particles or flakes whose sizes are comparable to the size of typical nozzles. This acoustic approach frees one from choosing only optically transparent (or weakly absorbing) and thermally stable materials. Second, high-speed jets (> 200 m/s) are readily attainable by taking advantage of bubble collapse, which can allow liquid injection to skins. Third, our jetting method is quite tolerable to a change in the position of the liquid surface within the acoustic focal length (approximately 500 μm), which makes our process more controllable

even when the liquid level is slightly changed for some reasons such as evaporation and jetting liquid consumption.

Based on the above advantages, our process can allow many potential applications. We demonstrated two possible applications, among others: printing and liquid injection into tissue mimicking materials.

[1] S. Mitragotri, Current status and future prospects of needle-free liquid jet injectors, Nat. Rev. Drug Discov. **5**, 543-548 (2006).
[2] M.R. Prausnitz, R. Langer, Transdermal drug delivery, Nat. Biotechnol. **26**, 1261-1268 (2008).
[3] F. Torrisi, T. Hasan, W. Wu, Z. Sun, A. Lombardo, T.S. Kulmala, G.-W. Hsieh, S. Jung, F. Bonaccorso, P.J. Paul, D. Chu, A.C. Ferrari, Inkjet-printed graphene electronics, ACS Nano **6**, 2992-3006 (2012).
[4] G. Percin, T.S. Lundgren, B.T. Khuri-Yakub, Controlled ink-jet printing and deposition of organic polymers and solid particles, Appl. Phys. Lett. **73**, 2375-2377 (1998).
[5] T.-H. Han, J.J. Yoh, A laser based reusable microjet injector for transdermal drug delivery, J. Appl. Phys. **107**, 103110 (2010).
[6] D.A. Fletcher, D.V. Palanker, Pulsed liquid microjet for microsurgery, Appl. Phys. Lett. **78**, 1933-1935 (2001).
[7] P.H. Chen, W.C. Chen, S.H. Chang, Bubble growth and ink ejection process of a thermal ink jet printhead, Int. J. Mech. Sci. **39**, 683-695 (1997).
[8] A. Antkowiak, N. Bremond, S. Le Dizes, E. Villermaux, Short-term dynamics of a density interface following an impact, J. Fluid Mech. **577**, 241-250 (2007).
[9] S. Gekle, J. Manuel Gordillo, D. van der Meer, D. Lohse, High-speed jet formation after solid object impact, Phys. Rev. Lett. **102**, 034502 (2009).
[10] Y. Tagawa, N. Oudalov, C.W. Visser, I.R. Peters, D. van der Meer, C. Sun, A. Prosperetti, D. Lohse, Highly focused supersonic microjets, Phys. Rev. X **2**, 031002 (2012).
[11] S.A. Elrod, B. Hadimioglu, B.T. Khuriyakub, E.G. Rawson, E. Richley, C.F. Quate, N.N. Mansour, T.S. Lundgren, Nozzless droplet formation with focused acoustic beams, J. Appl. Phys. **65**, 3441-3447 (1989).
[12] S.T. Thoroddsen, K. Takehara, T.G. Etoh, C.D. Ohl, Spray and microjets produced by focusing a laser pulse into a hemispherical drop, Phys. Fluids **21**, 112101 (2009).
[13] A. Patrascioiu, J.M. Fernandez-Pradas, J.L. Morenza, P. Serra, Film-free laser printing: jetting dynamics analyzed through time-resolved imaging, Appl. Surf. Sci. **302**, 303-308 (2014).
[14] A. Patrascioiu, J.M. Fernandez-Pradas, A. Palla-Papavlu, J.L. Morenza, P. Serra, Laser-generated liquid microjets: correlation between bubble dynamics and liquid ejection, Microfluid. Nanofluid. **16**, 55-63 (2014).
[15] H.W. Baac, J.G. Ok, A. Maxwell, K.T. Lee, Y.C. Chen, A.J. Hart, Z. Xu, E. Yoon, L.J. Guo, Carbon-nanotube optoacoustic lens for focused ultrasound generation and high-precision targeted therapy, Sci. Rep. **2**, 989 (2012).
[16] H.W. Baac, J.G. Ok, H.J. Park, T. Ling, S.L. Chen, A.J. Hart, L.J. Guo, Carbon nanotube composite optoacoustic transmitters for strong and high frequency ultrasound generation, Appl. Phys. Lett. **97**, 234104 (2010).

[17] See Supplemtal Material at http://link.aps.org/supplemental/--- for figures, discussions of surface tension effect and curved interface effect, and a animated image of jetting.
[18] T. Lee, D. Jang, D. Ahn, and D. Kim, Effect of liquid environment on laser-induced backside wet etching of fused silica, J. Appl. Phys. **107**, 033112 (2010).
[19] T. Lee, H.W. Baac, J.G. Ok, H.S. Youn, L.J. Guo, Controlled generation of single microbubble at solid surfaces by a nanosecond pressure pulse, Phys. Rev. Appl. **2**, 024007 (2014).
[20] H.W. Baac, T. Lee, L.J. Guo, Micro-ultrasonic cleaving of cell clusters by laser-generated focused ultrasound and its mechanisms, Biomed. Opt. Express **4**, 1442-1450 (2013).
[21] Y. Tomita, P.B. Robinson, R.P. Tong, J.R. Blake, Growth and collapse of cavitation bubbles near a curved rigid boundary, J. Fluid Mech. **466**, 259-283 (2002).
[22] B. Karri, S.R.G. Avila, Y.C. Loke, S.J. O'Shea, E. Klaseboer, B.C. Khoo, C.-D. Ohl, High-speed jetting and spray formation from bubble collapse, Phys. Rev. E **85**, 015303 (2012).
[23] K. Ando, A.-Q. Liu, C.-D. Ohl, Homogeneous nucleation in water in microfluidic channels, Phys. Rev. Lett. **109**, 044501 (2012).
[24] I.R. Peters, Y. Tagawa, N. Oudalov, C. Sun, A. Prosperetti, D. Lohse, D. van der Meer, Highly focused supersonic microjets: numerical simulations, J. Fluid Mech. **719**, 587-605 (2013).

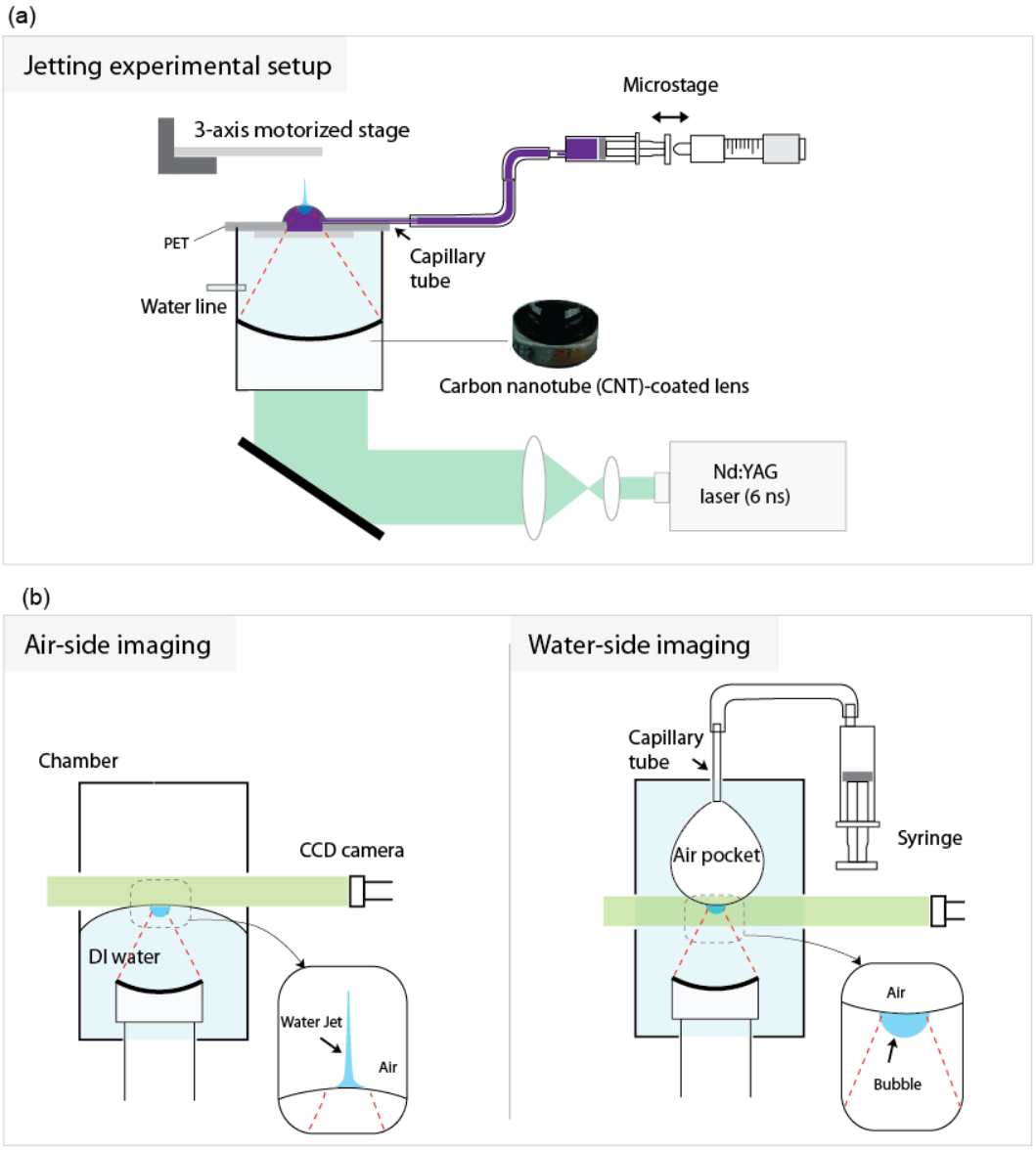

FIG. 1. (a) Experimental setup for bubble generation and liquid jetting. The focused optoacoustic wave is generated by pulsed excitation of the carbon-nanotube (CNT) optoacoustic transmitter (i.e., CNT lens). The jetting liquid fed through a capillary tube is separated from water by an acoustically transparent film. (b) Visualization of jetting with the air-side imaging setup where the chamber is overfilled with water, forming the free surface with a concave-down shape. Visualization bubble nucleation with the water-side imaging setup where the large air pocket forms the air-water interface with a concave-up shape.

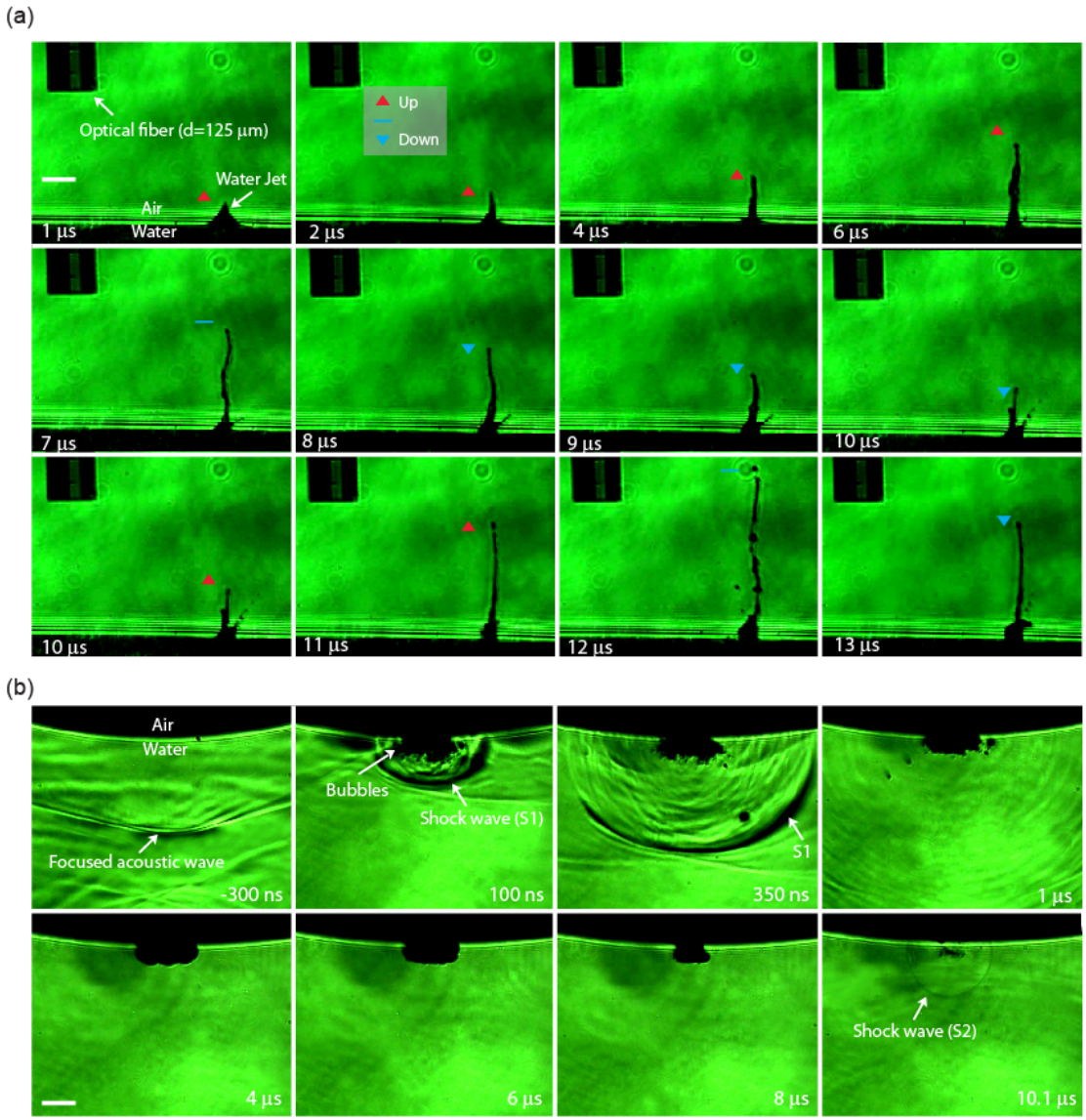

Fig. 2. Shadowgraph images of water micro-jets (a) and bubbles (b) at the air-water interface (laser energy E = 50 mJ/pulse). At the time t=0, the acoustic wave reaches the liquid interface. (a) Jet dynamics in the air side: the primary jets ($0<t<10$ μs) and the secondary jets ($t>10$ μs). The light-scattering objects such as the free surface with a concave-down shape, the jets, and the optical fiber look black, while the air is colored as green. The optical fiber (125 μm in diameter) is recorded as a reference object with a distance of approximately 350 μm from the free surface. The symbols indicate the up/down of the jets. The image for t=10 μs is repeated for easy comparison. (see Supplemental Material for an animated image [17]) (b) Bubble nucleation at the air-water interface. Note the change in the color scheme: the transmitted light through water is colored green, whereas the air pocket, bubbles, and shock waves that can scatter back-illuminating light are colored black. Two shock waves are observed: the primary shock wave (S1) generated by bubble nucleation, the secondary shock wave (S2) by collapse of the bubble. The bar indicates a length of 100 μm.

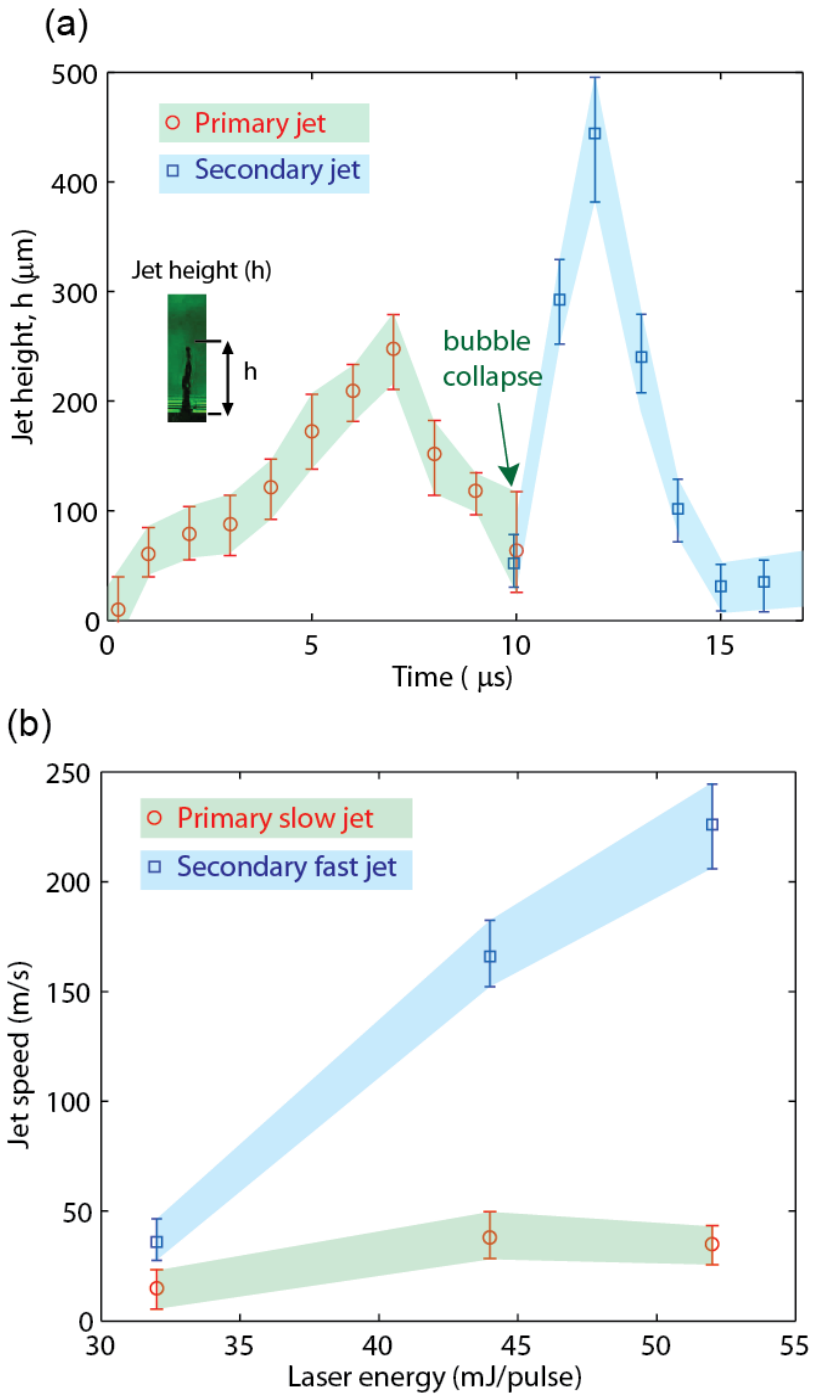

Fig.3. The characteristics of water micro-jets. (a) The height (h) of micro-jets as a function of time (E = 50 mJ/pulse). The two different jets indicated by shaded regions with different colors are observed before and after the bubble collapse: the primary slow jets (before the bubble collapse) and the secondary fast jets (after the bubble collapse). The bubble collapse is marked with a green arrow. (b) The jet speed as a function of laser energy (mJ/pulse). The primary jets with a relatively slow speed (symbol: red circle) induced by the bubble growth (up to V = 35 m/s). The secondary jets with a high speed (symbol: blue square) produced by the bubble collapse (up to V = 250 m/s). The markers represent averaged values, while the upper and lower errors show the maximum and minimum values.

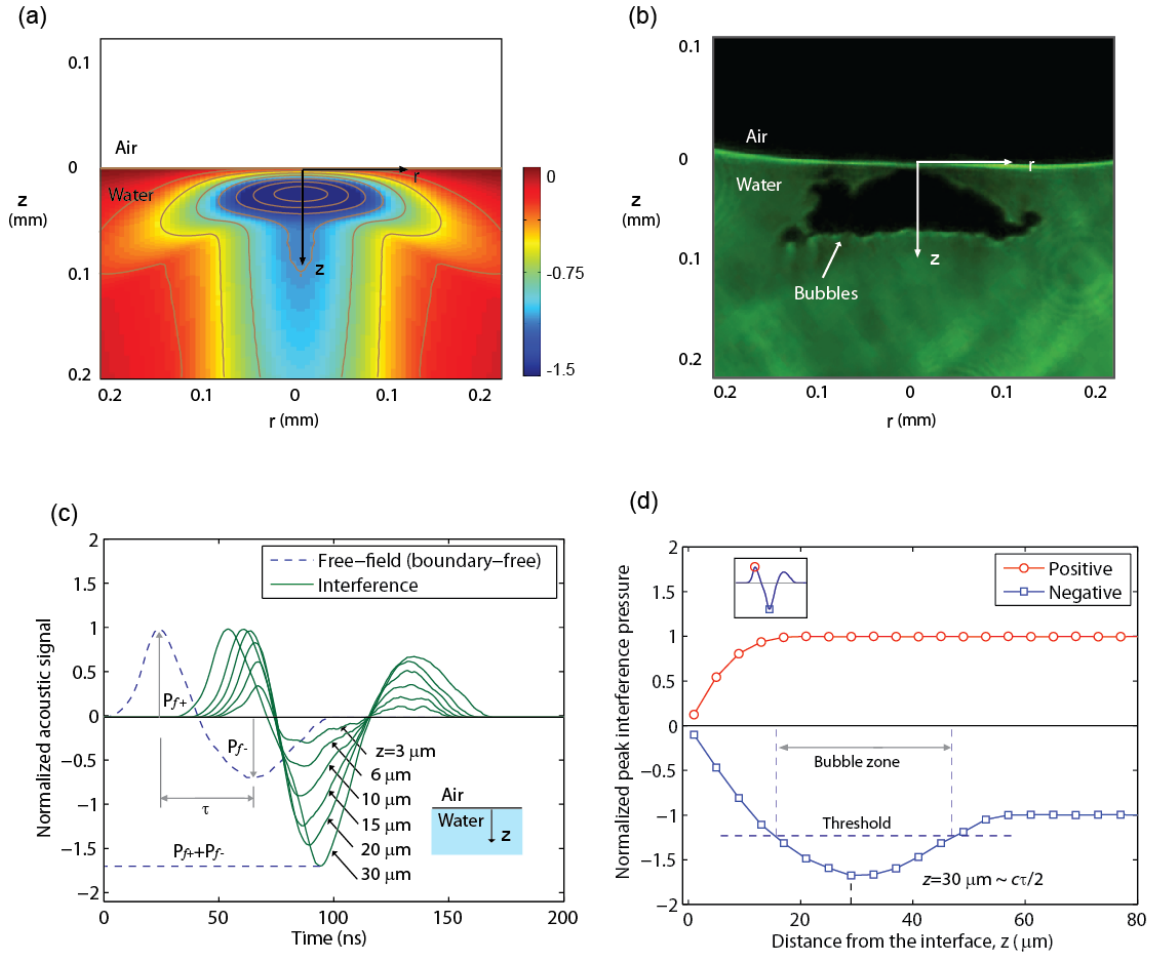

FIG. 4. Acoustic interference effect by the air-water interface. (a) The peak negative pressure field near the free surface (surface plot with contour lines, width x height = 400 μm x 200 μm), normalized to the maximum free-field negative amplitude. (b) The shadowgraph image of bubble nucleation zone (laser energy E = 50 mJ/pulse). (c) Normalized pressure transients for different distances form the interface (r = 0; z = 3, 6, 10, 15, 20, and 30 μm). The free-field pressure transient with a bipolar waveform (the positive amplitude = a, the negative amplitude = b, the peak-to-peak time delay = τ) is plotted with a dashed line. The maximum negative amplitude corresponds to the sum of the free-field positive and negative amplitudes (i.e., P_{f+}+P_{f-}). (d) Normalized negative (symbol: blue square) and positive peak amplitudes (symbol: red circle) as function of z. The maximum negative amplitudes at z_{max} = 30 μm (~ $c\tau$/2, where c is the speed of sound).

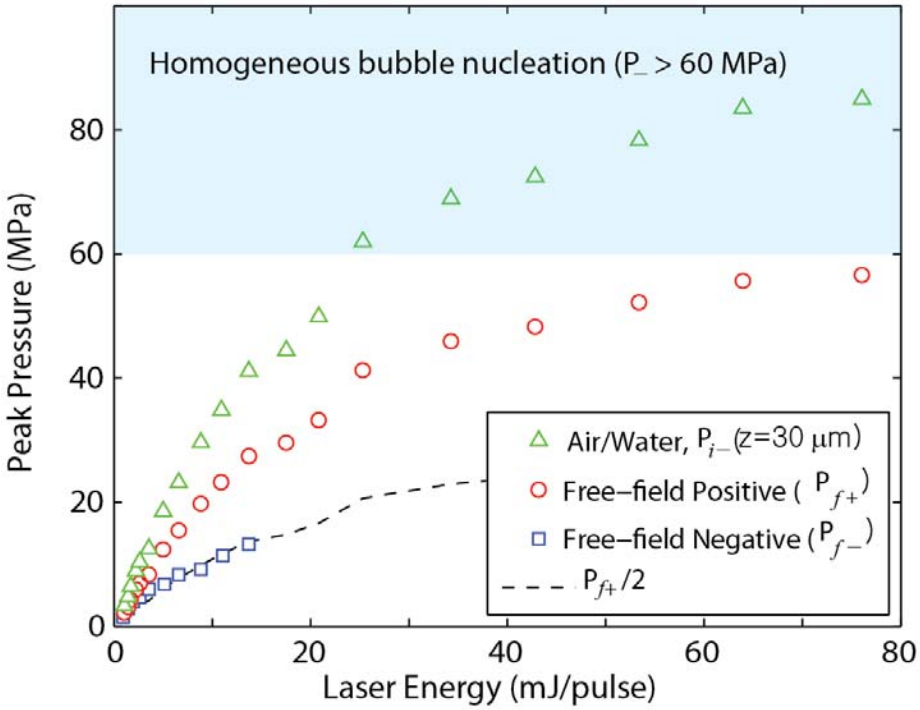

FIG. 5. Peak pressure amplitudes as a function of laser pulse energy. The measured free-field pressure amplitudes for negative (P_{f-}, blue square) and positive (P_{f+}, red circle). The interference negative pressure amplitudes (P_{i-}, green triangle) at z = 30 μm reconstructed from the free-field ($P_{i-} = P_{f+}+P_{f-} \sim 1.5P_{f+}$). The dashed line indicates half of the free-field positive amplitudes for estimating the free-field negative amplitudes ($P_{f-} \sim 0.5P_{f+}$). The shaded region indicates a region where the negative pressure amplitudes are higher than the homogeneous bubble nucleation threshold of water (> 60 MPa [21]).

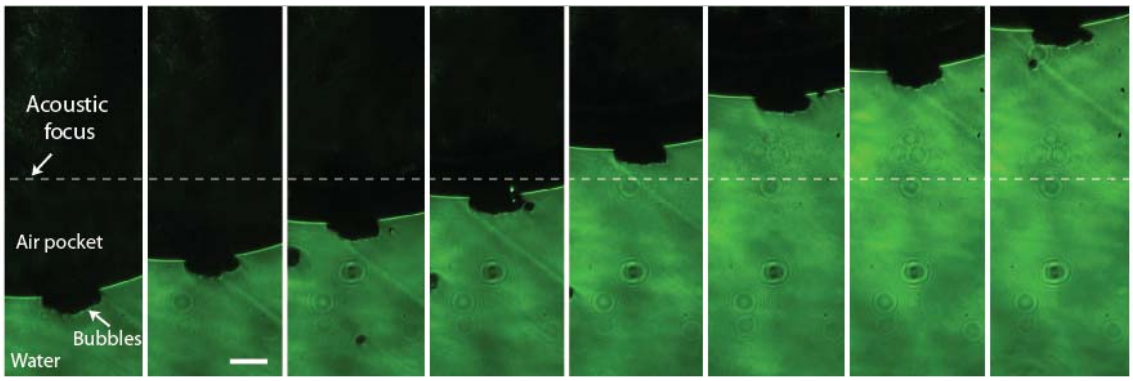

Fig. 6. Bubble nucleation tolerable to a change in the position of the free surface (E = 50 mJ/pulse). The acoustic focus indicated by a dashed line is fixed while by adjusting the position of the air pocket the air-water interface is moved up and down within the acoustic focal length (approximately 500 μm). All the images are captured 4 μs after the acoustic wave reaches the focus (dashed line). The scale bar indicates a length of 100 μm.

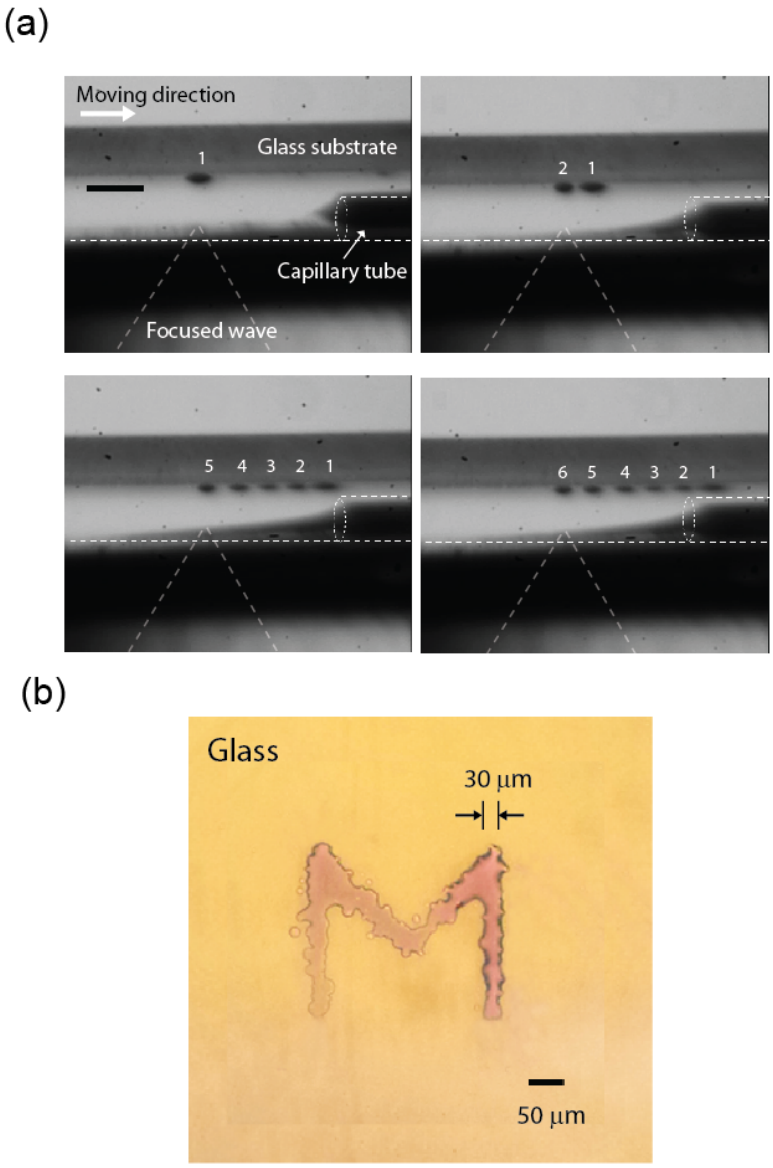

Fig. 7. (a) Liquid printing onto the glass substrate (E = 35 mJ/pulse). Each spot is made by multiple droplets while moving the glass substrate toward the right. The bar indicates a length of 500 μm. (b) Microscope image of the letter 'M' printed onto the glass substrate (E = 35 mJ/pulse). The line is a width of 30 μm, which is surrounded by liquid splashes or droplets. The bar indicates a length of 50 μm.

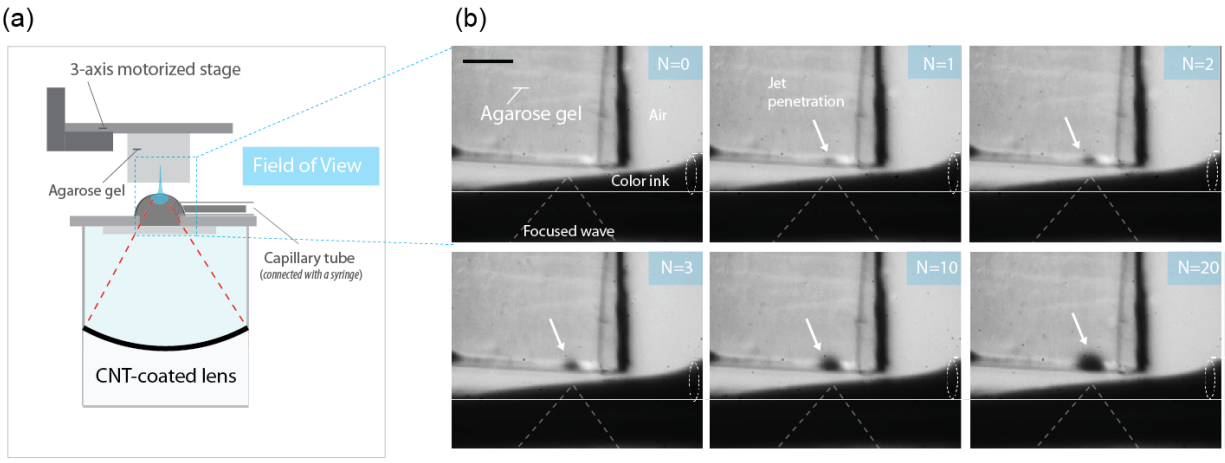

Fig. 8. Color ink injection into a tissue-mimicking material (agarose gel, thickness: 1 mm) at E = 50 mJ/pulse. The blue ink penetrates into the gel (marked as white arrows) for different number N of applied jets (N = 0, 1, 2, 3, 10, and 20). The bar indicates a length of 500 µm.